DTU Library

Comparison of Monolithic Optical Frequency Comb Generators Based on Passively Mode-Locked Lasers for Continuous Wave mm-Wave and Sub-THz Generation

Criado, A. R.; de Dios, C.; Acedo, P.; Carpintero, G.; Yvind, Kresten

Link back to DTU Orbit

Comparison of Monolithic Optical Frequency Comb Generators Based on Passively Mode-Locked Lasers for Continuous Wave mm-Wave and Sub-THz Generation

A. R. Criado, *Student Member, IEEE*, C. de Dios, P. Acedo, *Member, IEEE*, G. Carpintero, *Member, IEEE*, and K. Yvind

Abstract—In this paper, two different Passive Mode-Locked Laser Diodes (PMLLD) structures, a Fabry–Perot cavity and a ring cavity laser are characterized and evaluated as monolithic Optical Frequency Comb Generators (OFCG) for CW sub-THz generation. An extensive characterization of the devices under study is carried out based on an automated measurement system that systematically evaluates the dynamic characteristics of the devices, focusing on the figures of merit that define the optimum performance of a pulsed laser source when considered as an OFCG. Sub-THz signals generated with both devices at 60 GHz and 90 GHz are presented and analyzed in terms of electrical linewidth to compare such components for mm-Wave and sub-THz photonic generation. This work offers a systematic comparison of PMLLD devices for OFCG operation and provides reference information of the performance of two different device topologies that can be used for the implementation of photonic integrated sub-THz CW generation.

Index Terms—Mm-wave and THz photonic synthesis, optical filtering, optical frequency comb, optical heterodyne photomixing, passively mode-locked lasers.

I. INTRODUCTION

DURING the last decade, there has been a great research effort centered in the development of suitable generation and detection technologies to satisfy the needs of the frequency region known as the "THz gap" [1], [2]. This is mainly because of the great number of potential applications identified in this region, namely, imaging for security [3], [4] or biomedicine [5], spectroscopy [6] or short-range high data rate communications [7], among others. For some of them, even commercial room-temperature solutions for generation and/or detection are already available.

Nevertheless, there exists yet an important and increasingly need for even more compact, low cost and versatile solutions [8] that would allow complete exploitation of the THz domain with a more affordable technology This next generation of THz technology should be also energy-efficient, following the trend of all technology development nowadays, where the power consumption has become one of the main concerns [9], [10].

The Research and Development of technology for the THz region is being accomplished from two main approaches. The first one aims to push the frequency limits of electronic devices to cover the sub-THz and THz regions [11], while the second one is based on the downconversion from the optical domain [12]. Several schemes and technologies have been proposed and developed in the last years following both trends, but in terms of potential integration, compactness, performance and cost-effectiveness, which are the requirements for the next generation of THz technology; the main candidates nowadays are Resonant Tunneling Diodes (RTDs) for the electronic approach [13], and optical heterodyning using two optical frequencies for the photonic technology [14]. Both present advantages and disadvantages with respect to each other, but the optical heterodyning appears as a good candidate mainly because of two key aspects: a higher available bandwidth, both in generation [14] and detection [15]; and the integration potential as Photonic Integrated Circuit (PICs) using generic foundry platforms already available [16], [17].

Optical heterodyning relies on the combination in a photomixer device of two optical frequencies to generate an electrical signal with a frequency equal to the frequency spacing between both optical modes [14]. This electrical frequency must be within the bandwidth of the photomixer to properly achieve generation (highest output power). Suitable photomixer devices include photoconductive antennas (PCAs) [15], uni-travelling-carrier photodiodes (UTC-PDs) [18], travelling-wave uni-travelling-carrier photodiodes (TW-UTC-PDs) [19] or n-i-pn-i-p superlattice photomixers [20]. The two optical frequencies can be provided by two different sources (lasers) or by a single optical source. When two sources are used, continuous tunability is provided, but to obtain good phase noise characteristics of the generated signal complex optical phase-locked loops (OPLL) are needed to correlate the noise from both sources and attain a stable THz signal. In the case of using one source, this can be a dual-mode structure [21], where very limited tunability is offered, or a multimode optical source

(optical frequency combs), where discrete tunability (multiples of the fundamental repetition frequency) is provided using high selective optical filtering [22] or optical injection locking (OIL) [23] to select two modes from the optical spectrum. As the optical modes used for the THz signal generation are phase-locked and a narrow optical linewidth can be used, extremely low noise and narrow THz signals can be generated. Because of this, multimode sources are preferred for the development of high performance and compact THz generation technology.

Typical multimode sources are based on optical frequency comb generators (OFCGs) implemented as benchtop devices using phase modulators, non-linear fibers, RF generators and other external devices [18], [23], [24]. Nevertheless there are other devices, with much higher integration potential, that can be used as OFCG as are mode-locked laser diodes (MLLD) [22] or more recently, high-Q silicon-nitride spiral resonators [25]. While the latter resonators don't offer good phase noise characteristics and are not mature enough for integration, MLLDs are devices that can be integrated as PICs and are able to offer extremely low phase noise at less than 1 MHz offset from the carrier both under passive [26] regime and specially under active or hybrid regime [26]. Another advantage they offer is that the influence of mode partition noise is negligible because of the strong coherence that exists among the longitudinal modes emitted [27]. Thus, nowadays MLLDs are largely the best option for integrated GHz-rate OFCGs. Potential applications of these OFCG would include integrated systems requiring a fixed mm-wave carrier, as it is the case of automotive radars [28]; LO for integrated heterodyne receivers in the mm-wave and sub-THz region [29] or integrated OFCG for metrology [30].

When dealing with photonic generation of mm-wave and sub-THz signals, one of the fundamental parameter that has to be taken into account is phase noise. The electrical phase noise performance and linewidth of the sub-THz signals generated by actively mode-locked laser diode (AMLLD) or hybrid mode-locked laser diodes (HMLLDs) are inherited from the external RF reference used, that acts as a restoring force of the timing fluctuations, thus achieving extremely low phase noise and linewidths in the Hz range [26], [31]. In the case of passively mode-locked laser diodes (PMLLDs), also low noise performance is achieved, with linewidths below 1 kHz [26], but not as good as in the case of AMLLD or HMLLD [26], [32]. However, as no external RF reference is needed in the case of PMLLDs, just dc bias current for the gain section and DC reverse bias voltage for the saturable absorber, they make up a complete monolithic OFCG that in addition offers a dramatically reduction of power consumption, being the most efficient OFCG in terms of energy saving. In this sense, PMLLDs used as OFCG are great candidates for the development of the next generation of photonic THz transmitters technology that should be able to provide high performance and energy efficiency in an integrated and cost effective device.

The monolithic integration of PMLLD is a mature and fruitful field of study. The architecture most commonly considered is based on a travelling wave Fabry–Perot cavity [Fig. 1(A)]. In its simpler configuration, a Fabry–Perot PMLLD includes a gain section and an absorber section, though more complex and advanced structures have also been reported. Quantum well, quantum dot and quantum dash mode-locked lasers have
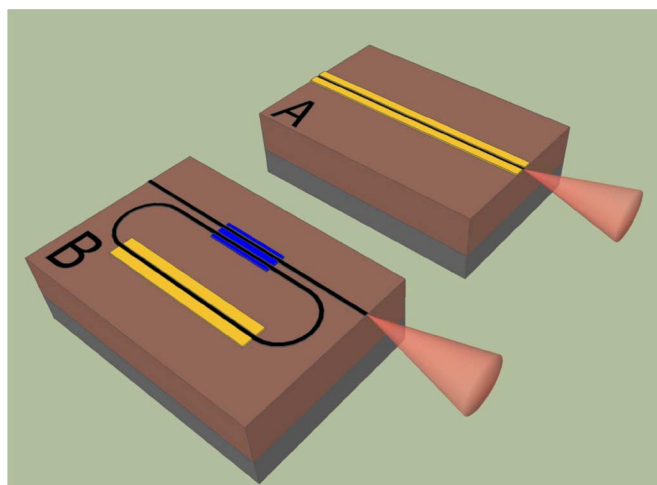

Fig. 1. Schematic view of (A) a Fabry–Perot laser cavity and (B) ring laser cavity. Yellow: gain regions and saturable absorbers; black: optical waveguides; blue: MMI optical coupler.

been manufactured using this design. As an alternative to those, monolithic devices based on ring cavity structures are being developed [Fig. 1(B)]. They provide with two important advantages over Fabry–Perot cavities. First, the length of the cavity can be more accurately controlled; and second, its output is coupled to a multimode interference (MMI) coupler also integrated in the substrate, allowing higher integration potential in PIC devices.

In this paper, and with the objective of experimentally identifying the optimum PMLLD structure for sub-THz integrated photonic generation, two different structures, a Fabry–Perot cavity (FP) PMLLD and a ring cavity PMLLD, are characterized and evaluated as monolithic OFCG for CW sub-THz generation. Both structures share the same material technology (InP) and are based on quantum well (QW) active regions. Systematic comparison of different operation parameters for both PMLLD devices is carried out to characterize them for optimum OFCG operation.

Generation of sub-THz signals using both devices at ∼60 GHz and ∼90 GHz is accomplished with the help of a photonic synthesis scheme based on the optical filtering of two modes from a multimode source and its photomixing in a high bandwidth photodiode [22]. The synthesized signals are evaluated in terms of electrical linewidth and compared to the reference information of the two different PMLLD topologies. The methodology described in this paper as well as the results on the comparison of both devices can be used to optimize PMLLD structures for the implementation of integrated sub-THz CW photonic generators.

II. CHARACTERIZATION OF MONOLITHIC OPTICAL FREQUENCY COMB GENERATORS BASED ON PASSIVELY MODE-LOCKED LASERS

A. Description of the Devices

The two PMLLDs structures that are to be evaluated in this work are represented in Fig. 1. As previously mentioned, the study will be centered only in PMLLDs given their potential features for the integration of CW THz transmitters. Both are
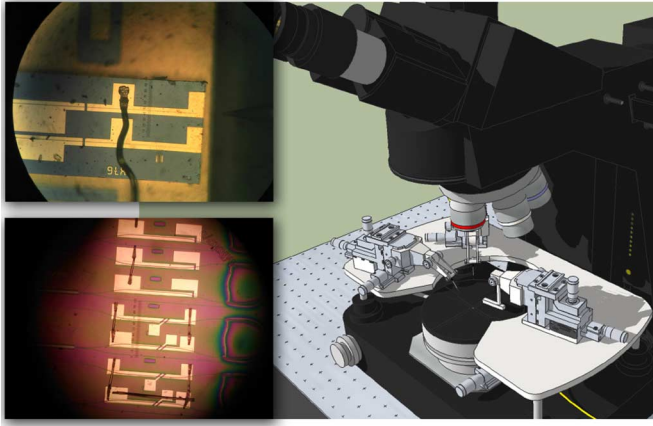
Fig. 2. Photograph of the chips containing the devices under test. PMLLD A (top) and PMLLD B (bottom) and their placement on the probe station.

QW-based devices. The first one has FP cavity [Fig. 1(A)] with a fundamental frequency set by the cavity round-trip time of f_A = 9.92 GHz (Device A, top of Fig. 2). The second one features a ring cavity structure [Fig. 1(B)] whose length gives a repetition rate of f_B = 14.99 GHz (Device B, bottom of Fig. 2).

Device A is a PMLLD that has been previously described in [33]. It has a two contact structure comprised of a Saturable Absorber (SA) section of 85 μm length and a gain section of 3915 μm length. The active region contains one InGaAsP/AlGaInAs QW emitting at a central wavelength of 1519 nm. Longitudinal confinement of the optical field is achieved by the formation of a 2 μm width ridge waveguide structure. The facet at the absorber end is HR coated (95% reflection) and the output facet is as cleaved [33].

Device B has been fabricated on an InP technology platform based on active/passive integration [16]. The active areas of the chip consist of four strained QWs embedded in 500 nm InGaAsP (Q1.25) waveguiding layer. The passive areas are formed by selective etching and re-growth, with a 500 nm InGaAsP (Q1.25) waveguiding layer, with buttjoint coupling to the active ones. Both the active and passive layers are sandwiched between an n-doped InP substrate and a p-doped 1500-nm-thick InP cladding with a 300 nm contact layer. Shallow etching is used for the straight waveguides while the curved waveguides are deeply etched. The shallow waveguides are created by an etch depth of 100 nm into the guiding layer, having a ridge width of 2 μm. The deep etched waveguides on the other hand have a ridge width of 1.5 μm. The ring structure that was measured has a total cavity length of 5405 μm, with an active section of 750 μm length in which a 30 μm long saturable absorber is defined at its center. The resulting repetition rate of the device is f_B = 14.99 GHz.

B. Characterization of the Devices

In this section, a complete characterization of the two devices is presented, with emphasis on the parameters of interest for proper OFCG operation.

The experimental setup for the measurement of the devices is depicted in Fig. 3. The output of the laser is coupled to a lensed
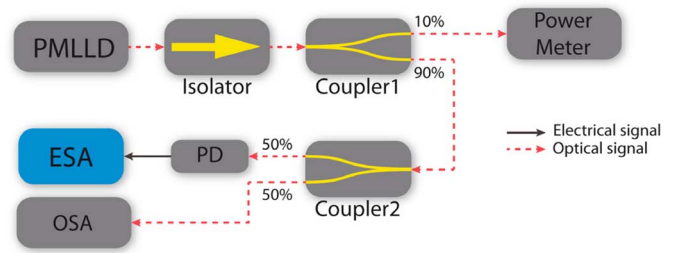

Fig. 3. Experimental setup for devices characterization.

fiber followed by an optical isolator. A 10% of the signal is coupled out (Coupler1) for power monitoring, while the rest is divided by a 3-dB optical coupler (Coupler2). One of the outputs is monitored in an OSA. The second output is downconverted from optical to electrical domain using a high bandwidth photodiode (PD) (50 GHz 3-dB bandwidth) and monitored in an ESA.

PMLLDs characterization and their qualitative analysis are presented in three steps using the data provided by the characterization platform described. Step 1) aims for a general description of the performance of the devices based on six figures of merit (parameters) that are detailed in corresponding maps for the operational range of the devices defined by the bias current into the active region (I) and the reverse voltage in the saturable absorber (V). Then, in step 2), a detailed analysis for the optimum saturable absorber voltage (V) value obtained in step 1) is carried out. Finally, step 3), deals with the detailed characterization of the optimum V-I point for each device identified in steps 1) and 2).

Step 1) To proceed with the first characterization stage, the data maps for six OFCG figures of merit (parameters) are presented in Fig. 4. The measurements can be classified in two categories: optical domain characteristics and electrical domain characteristics. The optical parameters are measured using an Optical Spectrum Analyzer (OSA, Fig. 3) and those are the output optical power, the central wavelength and optical full width at half maximum (FWHM) values. The electrical domain measurements are measured using and ESA, Fig. 3) connected at the output of the high speed photodiode used for detecting the optical signal from the devices. Those electrical parameters are the beat electrical power, beat electrical frequency and electrical FWHM. These six parameters are evaluated for several gain section currents (I) and saturable absorber voltages (V), within the safety limits of the devices, to obtain six maps that allow identification of the different working regions for each device (Fig. 4).

The behavior of device A is depicted in Fig. 4(a). From these results we can conclude that the behavior of the device used as OFCG improve when both current and reverse voltage increases, leading to a clear region located at the higher reverse voltage and current levels where the device offers a better performance [Fig. 4(a)]. In the case of device B [Fig. 4(b)],
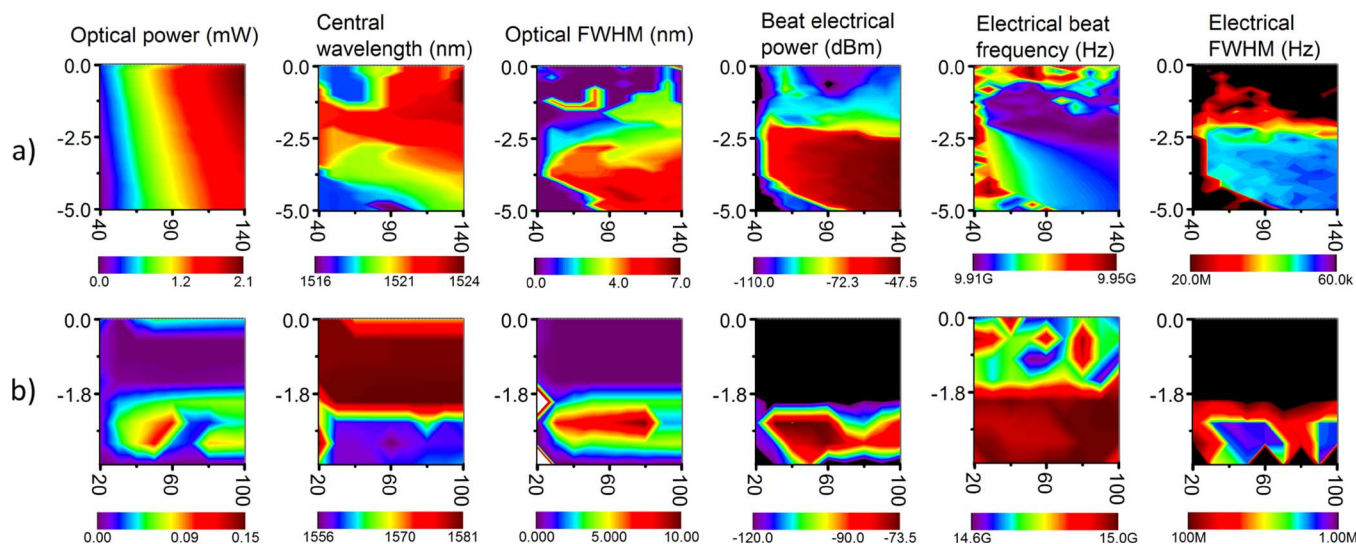
Fig. 4. V-I OFCG figure-of-merit maps for device A (top row) and device B (bottom row). Gain section current (I) is in mA (horizontal axis) and saturable absorber voltage (V) is in volts (vertical axis). Z-axis scales: Optical power (linear), Central wavelength (linear), Optical FWHM (linear), Beat electrical power (logarithmic), Electrical beat frequency (linear), electrical FWHM (logarithmic).

there exists a more specific region, around -2.5 V and 50–90 mA, where the device features its best performance (i.e., higher power and optical FWHM and narrower electrical FWHM). In this case that region does not correspond to the lowest voltage and highest current values.

The optical power output for device A reaches as much as 2 mW, increasing linearly as a function of the bias current. Device B has a much lower output power, showing a maximum of 0.1 mW for the operational region centered at 50 mA and -2.5 V. From the optical measurements, it can be seen that the threshold currents are approximately 40 mA and 20 mA for devices A and B, respectively.

The wavelength of device A is slightly outside the telecom range (1550 nm), centered around 1520 nm, while in the case of the device B, we have two completely different regions of operation as far as for the central wavelength is concerned. Above -2 V the central wavelength is centered at 1580, while below this value, the optical spectrum "hops" into the 1556 nm region. The optical comb-like spectra reaches a FWHM value of around 6 nm ($\sim$0.8 THz) for device A, increasing as both current and reverse voltage increase; while the device B presents a FWHM value of around 9 nm ($\sim$1.2 THz) in the region below -1.8 V.

The evolution of the electrical domain parameters evaluated follows a similar trend as the optical figures of merit. Device A presents a beat signal with a frequency around 9.92 GHz and with an electrical power that increases with current and reverse voltage. Device B has an electrical beat of a frequency around 14.99 GHz and a maximum power of -73 dBm that is observed in a small region centered over 50 mA and -2.5 V.

With this first set of data we are able to identify the V-I operation regions where the devices will behave better as OFCGs. These regions would be the V-I region above 60 mA and below -2.5 V for PMLLD A; and above 25 mA and below -1.8 V for PMLLD B.

Step 2) The mapping of the different figures of merit described above has allowed us to identify the optimum saturable absorber reverse voltage for both devices. Now in this second step, the saturable absorber voltages for both devices are kept constant at the values where the previously described figures of merit present better values, this is, -4 V for PMLLD A and -2.5 V for PMLLD B. For further characterization of the devices, the above mentioned figures of merit are represented again in 2D graphs as a function of the bias current (Fig. 5) for those optimum voltage values. This gives a clearer and more comprehensive view of the performance offered by the devices at its optimum voltage point and permits the identification of the optimum bias current point.

Fig. 5(a) presents the OFCG figures of merit for device A. It can be seen again that the optical output power has a linear dependence with the bias current after the threshold current, which has a translation in the electrical beat power that also increases with the current. In Fig. 6(a) the evolution with the bias current of the optical and electrical spectra are shown, where we can see a continuous tunability range between 1517.02 to 1520.4 nm for the central wavelength of the optical comb, and between 9.932 and 9.921 GHz for the beat frequency. The optical FWHM is almost constant after 70 mA within the range between 4.9 to 5.7 nm; while the electrical FWHM decreases when the current rises, to then stabilize for high current values ($>$100 mA), at around a minimum value of 185 kHz.
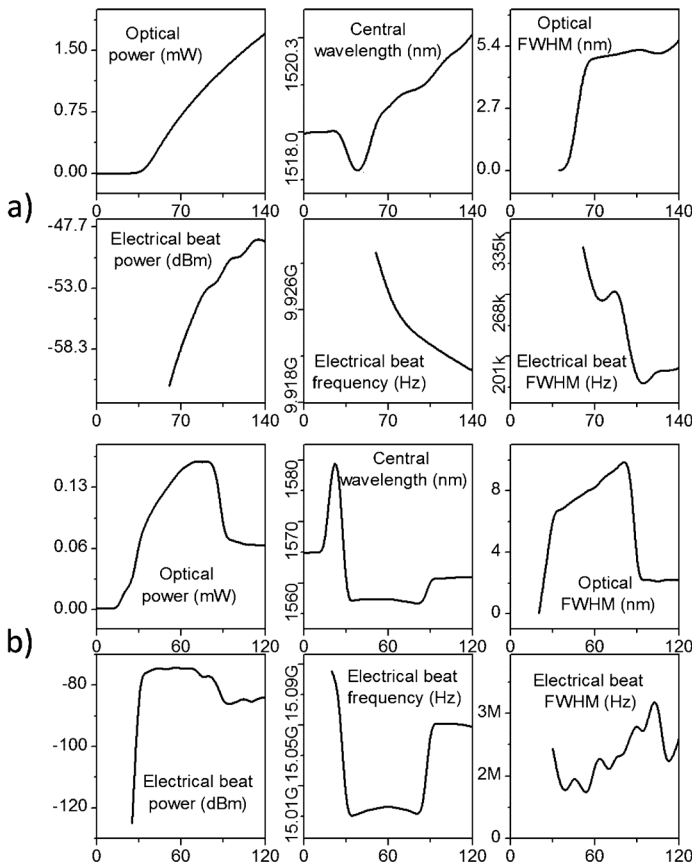
Fig. 5. Evolution of the electrical and optical figures of merit as a function of the bias current (horizontal axis, I, mA) for A and B for optimum saturable absorber voltages: −4 V and −2.5 V, respectively.
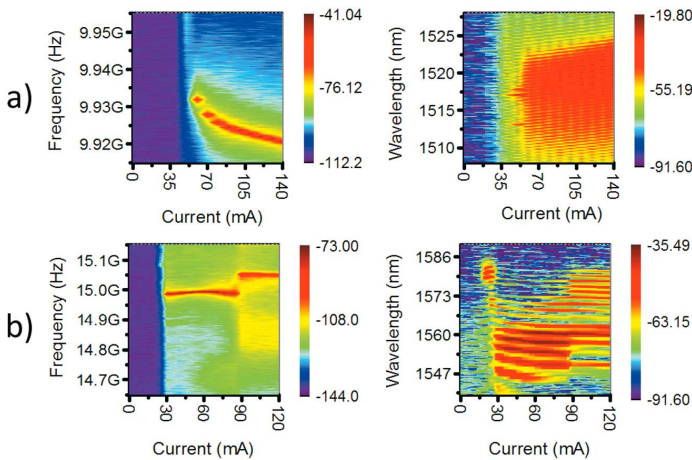

Fig. 6. Electrical and optical spectra evolution with bias current for devices A and B for optimum saturable absorber voltages: −4 V and −2.5 V, respectively. Z axis units are dBm.

In Fig. 5(b) the merit figures for device B are represented. In this case, there is an increment of both optical and electrical beat power with the current below 70 mA. Above this point, the power saturates and begins to decrease, limiting the proper working region to 20–70 mA. Near this region (30–80 mA), a comb-like spectra centered at 1556 nm appears as
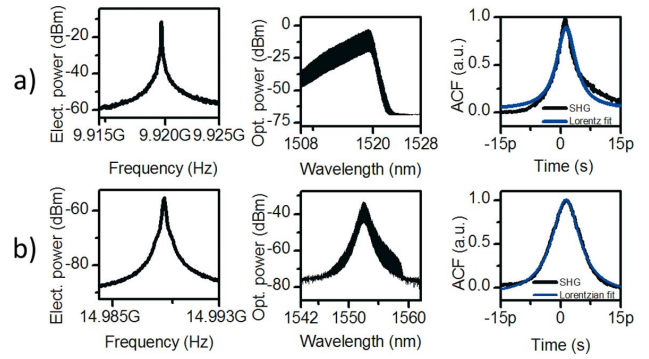

Fig. 7. Electrical beat signal at fundamental frequency (first column), bandpass filtered optical spectra (second column) and SHG autocorrelation trace (third column) for device A (a) and device B (b).

dominant in the optical spectra, as it can be appreciated in Fig. 5(b) and in Fig. 6(b). The beat frequency in this working range (30–80 mA) decreases to 14.99 GHz, remaining almost constant. The optical FWHM reaches 9 nm of maximum value and the electrical FWHM of the beat note has a minimum value of 1.5 MHz.

Step 3) Characterization steps 1) and 2) have allowed us to identify the optimum V-I working points for both devices that are −4 V and 140 mA for device A and −2.5 V and 50 mA for device B. In this final characterization step, we proceed to fully evaluate the performance of both devices as OFCG for mm-wave and sub-THz generation.

In this sense, the optical outputs from both devices at their optimum operation points are also characterized in terms of the temporal width of the generated pulses using a Second Harmonic Generation (SHG) autocorrelator. Given the low efficiency of the SHG process and the low output power of the devices, the optical output from both devices is amplified using an Erbium Doped Fiber Amplifier (EDFA) and filtered with Optical Band Pass Filters (OBPF) for ASE suppression. Due to the different emission wavelength presented by both devices, different EDFAs and optical filters had to be used to perform the measurements. The results are shown in Fig. 7. The optical spectra under these conditions and the generated electrical beat after photomixing are also displayed, along with the autocorrelation trace for comparison (Fig. 7).

The temporal traces obtained from the fitting of the autocorrelation traces with the autocorrelation of Lorentzian functions (Fig. 7) provides temporal FWHM values of 5.8 ps for device A and 8.57 ps for device B. The values for the Time-Bandwidth Product (TBP) are computed using the bandwidth determined by the ASE suppression filtering stages and are shown in Table I. A summary on other electrical and optical characteristics of both devices in their optimum V-I point is presented in Table I. In

TABLE I
FIGURES OF MERIT SUMMARY

| PARAMETER/DEVICE	A	B
OPTIMUM V-I POINT, OPTICAL AMPLIFYING + FILTERING (FIG. 7) FIGURES OF MERIT VALUES		
Central wavelength (nm)	1520	1558
Optical FWHM (without filtering) (nm/GHz)	5.7/740	7.7/952
Optical FWHM (with filtering) (nm/GHz)	1.5/195	1/124
Beat signal frequency (Hz)	9.92G	14.99G
Electrical beat power (dBm)	-11.7	-56.6
Electrical beat FWHM (Hz)	59.1k	430k
Temporal width (ps)	5.8	8.57
TBP	1.13	1.06
NO OPTICAL AMPLIFYING, NO OPTICAL FILTERING (FIGS. 3 TO 6) ABSOLUTE BETTER VALUES OF THE FIGURES OF MERIT		
Maximum optical power (mW)	2.1	0.15
Maximum optical FWHM (nm/GHz)	6.3/814	9.1/1229
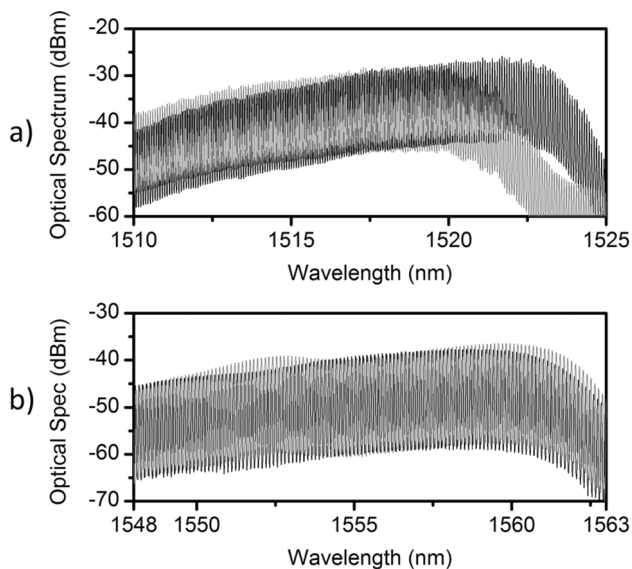
Fig. 8. Optical spectra showing the optical FWHM for the optimum V-I point (black line) and the absolute maximum optical FWHM (grey). Device A (a) and device B (b).

this Table I, also the absolute higher values of both optical power and optical FWHM are included.

As mentioned before, these devices are planned to be used for mm-wave and sub-THz generation. To evaluate the maximum frequency that could be synthesized with both OFCG, the absolute maximum optical FWHM of the devices (Maximum optical FWHM in Table I) along with their optical FWHM in the V-I point determined as optimum (Optical FWHM (without filtering) in Table I) are shown in Fig. 8. Signals up to 814 GHz (Maximum optical FWHM of Device A in Table I) and up to 1229 GHz (Maximum optical FWHM of Device B in Table I) can be synthesized provided a sufficient bandwidth photomixer [18]–[20].

C. Algorithm for Calculation of the Global Performance Maps of the Devices as Optical Frequency Comb Generators

In the previous paragraphs we have performed a systematic and exhaustive analysis of two PMLLD to evaluate them as

OFGCs for sub-THz generation that has included the evaluation of several parameters and a three steps process to identify the best operation points for them and characterize the performance of the devices for those points. This process is tedious and may take a lot of time that is not efficient when several devices of slightly different characteristics are to be evaluated.

In this sense, and with the aim to provide ourselves with a more efficient way to characterize different PMLLDs for mm-wave and sub-THz generation, we have developed an algorithm that provides directly with a Global Performance Map for the devices, in this case to evaluate their performance as OFCG. The algorithm gives a mark to each V-I point based on a criteria adapted to the actual application that will have the device. The criteria are user configurable. For the particular study presented in this work, and based on the detailed discussion described in the previous section, we are ready to define a criteria oriented to evaluate the optimum operation point of a PMLLD when considered as an OFCG. The resulting maps allow a direct and quantitative identification of the optimum V-I points for OFCG operation. Furthermore, the mark values can be referred to a common reference scale, allowing us to evaluate PMLLDs with different characteristics (i.e., gain regions, cavity structures). This provides us with a useful, fair and accurate comparison indicator across devices with different characteristics.

From the different figures of merit evaluated above, the Global Performance (GP) Indicator, i.e., the mark value assigned to each V-I point, is calculated as follows:

$$\text{GP}_i = \prod_j \left\{ \frac{MF_{ij} - \min\left(mMF_j\right)}{\max\left(MMF_j\right) - \min\left(mMF_j\right)} \right\}^{w_j} \quad (1)$$

where

$$mMF_j = \left\{\min(MF_{ij})\right\}_{i=1}^N \quad (2)$$

$$MMF_j = \left\{\max(MF_{ij})\right\}_{i=1}^N . \quad (3)$$

That is, the Global Performance indicator (GP_i) for a device i is computed as the product of all its figures of merit described above $(MF_{i,j})$, where each one is normalized between the minimum (2) and the maximum (3) figure of merit values for all the compared devices. An exponential weighting factor (w_j) is applied to each figure of merit normalized this way. The absolute value for this weighting factor accounts for the relevance of that figure for the intended application (OFCG in this case), and the sign discriminates if a higher value of the figure is preferred (positive sign) or a lower value is preferred (negative), as it is the case of the electrical FWHM for OFCG application. A product has been chosen instead of a sum to have a sharper identification of different performance areas.

For this analysis, a value of 1 has been chosen for optical power, electrical power and optical FWHM. Both, beat frequency and central wavelength, have been assigned with a weight of 0 (i.e., not relevant), while the electrical FWHM has a weight of −1.

The GP indicators for both devices under study, normalized to a common scale between 0 and 100, are presented in Fig. 9 in a logarithmic scale. Device A obtains a much better performance mark in this case, mainly because of the better electrical FWHM and especially because of the optical and electrical power that is able to deliver. It must be noted that if a higher weight is
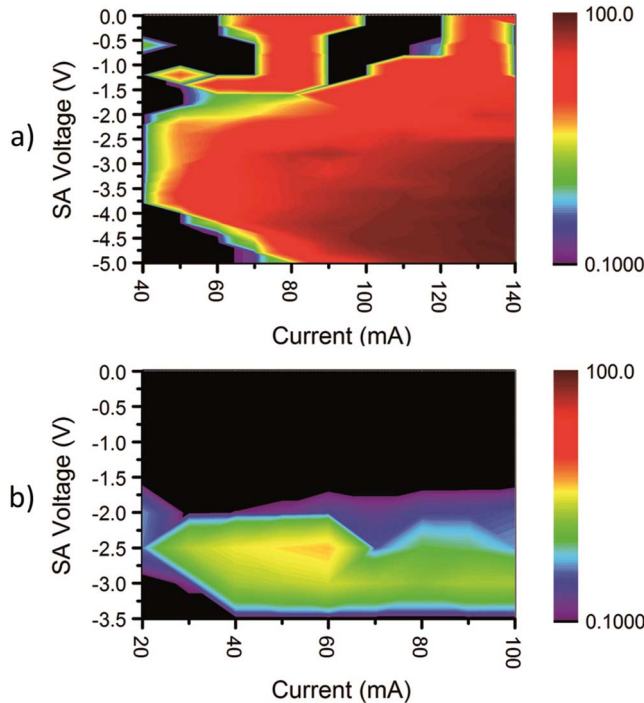
Fig. 9. OFCG performance maps for (a) PMLLD A and (b PMLLD B using the same reference scale (logarithmic scale).
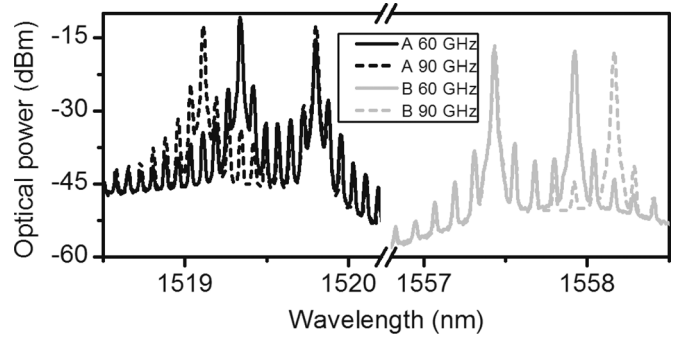

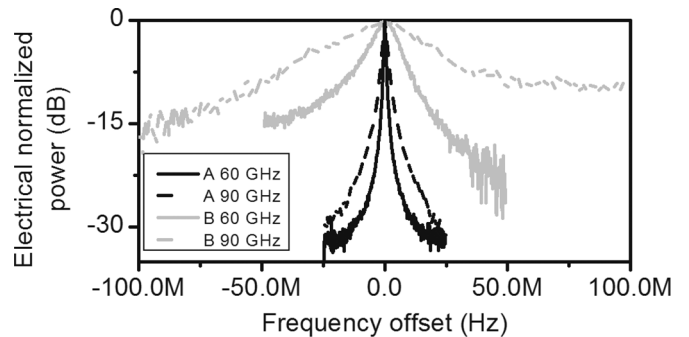Fig. 10. Filtered optical spectra with the selected longitudinal optical modes for the generation of the sub-THz CW signal.

Fig. 11. Electrical spectra of the sub-THz CW signals generated after photomixing the optical spectra in Fig. 10 in a photomixer.

assigned to the optical span, which would be another possible scenario for the evaluation of an OFCG, device B would have a much higher mark, given the wide optical span it is able to provide (up to 1.2 THz).

III. SUB-THz CONTINUOUS WAVE SIGNALS GENERATION WITH MONOLITHIC OPTICAL FREQUENCY COMB GENERATORS BASED ON PASSIVELY MODE-LOCKED LASERS

As mentioned in the Introduction, the final objective of this work is to propose a systematic way to evaluate different PMLLD to be used as OFCG for mm-wave and sub-THz generation comparing two different PMLLD structures using a proposed Global Performance map. In this sense, the final step of this work must be the use of such devices for CW sub-THz photonic generation employing them as OFCG in an optical heterodyning scheme, and to compare the actual characteristics of the synthesized signals (quality) with the outcomes from the previous analysis.

As stated in the Introduction, a PMLLD is suitable to be used as OFCG in any optical heterodyning setup based on the photomixing of two longitudinal modes from a multimode source, like those described on [18], [22], [23]. For the analysis presented here, the scheme reported in [22] based on optical filtering is used. In this case, the selection of the optical modes from the OFCG for sub-THz signal generation is attained by using high selectivity Fabry–Perot Tunable Fiber Filters while the photomixing is accomplished using a high bandwidth photodiode (50 GHz 3-dB bandwidth). Optical amplification with two EDFAs is used to have an optical power at the input of the photodiode equal to its maximum average optical input power

(13 dBm). In this case the employed photomixer is the limiting factor because of its 50-GHz bandwidth and thus the analysis will be restricted to the synthesis of CW signals at $\sim$60 and $\sim$90 GHz. Nevertheless, the results at those mm-wave frequencies will be sufficient for the study of the electrical linewidth and spectral shape of the synthesized signals, and to determine the differences between the signals produced from both PMLLDs.

The bias conditions for the PMLLDs correspond to the optimum working points identified in the analysis from Section II, this is, -4 V and 140 mA for device A, and -2.5 V and 50 mA for device B. In Fig. 10, the optical spectra after the high selectivity filtering stage to select the longitudinal optical modes from the OFCG before photomixing, are represented. The optical spectrum corresponding to device A is depicted in black, while that from device B is presented in grey. For both devices the beating of the optical spectra displayed in solid trace will generate the $\sim$60 GHz CW signal in the photodiode; and the spectra in dashed trace, the $\sim$90 GHz CW signal. More specifically, the generated frequencies will correspond to $n \cdot f_i$, where n is the number of modes of separation between the selected longitudinal modes, and f_i the fundamental frequency associated to each device (59.52 GHz and 89.28 GHz for device A; 59.96 GHz and 89.94 GHz for device B). The Side Mode Suppression Ratio (SMSR) for device A is around 12 dB and increases up to almost 20 dB for device B because of the higher frequency spacing.

In Fig. 11, the normalized sub-THz signals synthesized with both monolithic OFCGs at $\sim$60 and $\sim$90 GHz are represented.

The measurements are limited by the low power of the generated signals and especially by the low dynamic range of the measurement system mainly caused by the conversion losses of the harmonic mixers employed for the downconversion as well as the operation beyond the bandwidth of the photodiode. For device A, the electrical output powers corrected for the losses of the harmonic mixers are -42 dBm and -35 dBm for 60 GHz and 90 GHz, respectively. The signals generated with device B have an electrical power of -61 dBm (60 GHz) and -68 dBm (90 GHz).

The differences in the dynamic range for the different measurements has as a consequence that a fair comparison of the electrical performance should be based on the electrical linewidth rather than on the SSB noise [22]. Accordingly, the analysis of the performance of the photonically synthesized signals will be based mainly in the electrical FWHM. From the results of Fig. 11 we can see that device A provides a much narrower linewidth, performing a FWHM of 843 kHz at 60 GHz and 1.96 MHz 90 GHz. For its part, the sub-THz signals synthesized with device B present 10.5 MHz at 60 GHz and 32.2 MHz at 90 GHz. The increment in the linewidth as the frequency increases is within the expected range for a PMLLD [32].

Again, it must be noted that the maximum frequency of the synthesized signals is limited both by the bandwidth of the OFCGs (around 800 GHz and 1.2 THz of 3-dB bandwidth for our OFCG A and B, respectively) and by the photomixer bandwidth. The photodiode used in this experiment has a maximum optical input power of 20 mW and a 3-dB bandwidth of 50 GHz and it is clearly limiting the performance above 90 GHz regardless the high bandwidth available associated to our OFCGs. However, as previously mentioned, state of the art photomixers can reach values up to 1 THz in the case of Uni-Travelling-Carrier Photodiodes (UTC-PD) [18], Travelling-Wave Uni-Travelling-Carrier Photodiodes (TW-UTC-PD) [19] or n-i-pn-i-p superlattice photomixers [20]. Hence, the proposed scheme can be readily scaled to synthesize higher frequencies.

These results regarding the sub-THz CW photonic synthesis agree well with the systematic analysis and comparison presented in Section II, and especially with the use of the defined GP indicators to evaluate the performance of PMLLD as OFCG for sub-THz signal synthesis when used in an optical heterodyning setup based in multimode source for CW sub-THz generation.

IV. CONCLUSION

This work provides with reference information of the performance of two different PMLLD topologies that can be used for the implementation of the next generation of integrated sub-THz CW photonic generation technology based on PICs. With this aim, two different PMLLDs are characterized and evaluated as monolithic OFCG for CW sub-THz generation.

Firstly, an exhaustive characterization and analysis of both devices is carried out. It is focused in the figures of merit of an OFCG. A specific characterization platform has been implemented for this, providing all the measurement data and computing a Global Performance (GP) map for each device that al-

lows a direct identification of the optimum working points for an specific application (in this case OFCG), based on a quantitative analysis whose criteria is user configurable. The algorithm computes the GP indicator referred to a common scale for all the devices under study, allowing a fair an accurate comparison between devices with different characteristics.

Secondly, the devices have been employed in a sub-THz CW photonic synthesis scheme for the generation of signals at $\sim$60 GHz and $\sim$90 GHz. This allows validating the application of this kind of devices for sub-THz generation. The signals are analyzed and evaluated in terms of electrical linewidth and the results for both devices serve us to validate the Global Performance predicted in the first part and validate the proposed systematic analysis and comparison between devices.

Device A, which has a one-QW straight Fabry–Perot cavity, gets a better overall performance, and provides with narrower linewidth sub-THz synthesized signals than device B, which features a four-QW ring cavity. Nevertheless there are two important points where device B provides better features: the maximum optical span it can offer (up to 1.2 THz), and the advantages given by its cavity design (much higher integration potential in a PIC and more accurate fabrication of the cavity length).

REFERENCES

[1] P. H. Siegel, "Terahertz technology," *IEEE Trans. Microw. Theory Tech.*, vol. 50, no. 3, pp. 910–928, Mar. 2002.

[2] M. Tonouchi, "Cutting-edge terahertz technology," *Nat. Photon.*, vol. 1, pp. 97–105, 2007.

[3] C. Jansen, S. Wietzke, O. Peters, M. Scheller, N. Vieweg, M. Salhi, N. Krumbholz, C. Jördens, T. Hochrein, and M. Koch, "Terahertz imaging: Applications and perspectives," *Appl. Opt.*, vol. 49, pp. E48–E57, 2010.

[4] W. R. Tribe, D. A. Newnham, P. F. Taday, and M. C. Kemp, "Hidden object detection: Security applications of terahertz technology,". San Jose, CA, 2004, pp. 168–176.

[5] P. H. Siegel, "Terahertz technology in biology and medicine," *IEEE Trans. Microw. Theory Tech.*, vol. 52, no. 10, pp. 2438–2447, Oct. 2004.

[6] P. F. Taday, "Applications of terahertz spectroscopy to pharmaceutical sciences," *Philos. Trans. Royal Soc. London A, Math., Phys. Eng. Sci.*, vol. 362, pp. 351–364, Feb. 15, 2004, 2004.

[7] R. Piesiewicz, T. Kleine-Ostmann, N. Krumbholz, D. Mittleman, M. Koch, J. Schoebel, and T. Kurner, "Short-range ultra-broadband terahertz communications: Concepts and perspectives," *IEEE Antennas Propag. Mag.*, vol. 49, no. 1, pp. 24–39, Jan. 2007.

[8] "A new phase for THz," *Electron. Lett.*, vol. 47, pp. 1255–1255, 2011.

[9] R. S. Tucker, "Green optical communications—Part I: Energy limitations in transport," *IEEE J. Sel. Topics Quantum Electron.*, vol. 17, no. 2, pp. 245–260, Mar.–Apr. 2011.

[10] R. S. Tucker, "Green optical communications—Part II: Energy limitations in networks," *IEEE J. Sel. Topics Quantum Electron.*, vol. 17, no. 2, pp. 261–274, Mar.–Apr. 2011.

[11] H. W. Hubers, "Terahertz heterodyne receivers," *IEEE J. Sel. Topics Quantum Electron.*, vol. 14, no. 2, pp. 378–391, Mar.–Apr. 2008.

[12] T. Nagatsuma, "Generating millimeter and terahertz waves," *IEEE Microw. Mag.*, vol. 10, pp. 64–74, 2009.

[13] M. Feiginov, C. Sydlo, O. Cojocari, and P. Meissner, "Resonant-tunnelling-diode oscillators operating at frequencies above 1.1 THz," *Appl. Phys. Lett.*, vol. 99, 2011, Art. ID 233506.

[14] S. Preu, "Tunable, continuous-wave Terahertz photomixer sources and applications," *J. Appl. Phys.*, vol. 109, p. 061301, 2011.

[15] A. Masaaki, A. Ryota, S. Hiroshi, K. Ikufumi, I. Tadashi, M. Katsuhiko, and I. Hiromasa, "Ultrabroadband THz field detection beyond 170 THz with a photoconductive antenna," in *Proc. CLEO*, 2008, paper CTuX6.

[16] X. Leijtens, "JePPIX: The platform for indium phosphide-based photonics," *IET Optoelectron.*, vol. 5, pp. 202–206, 2011.

[17] L. A. Coldren, S. C. Nicholes, L. Johansson, S. Ristic, R. S. Guzzon, E. J. Norberg, and U. Krishnamachari, "High performance INP-based photonic ICs—A tutorial," *J. Lightw. Technol.*, vol. 29, no. 4, pp. 554–570, Feb. 2011.

[18] S. Ho-Jin, N. Shimizu, T. Furuta, K. Suizu, H. Ito, and T. Nagatsuma, "Broadband-frequency-tunable sub-terahertz wave generation using an optical comb, AWGs, optical switches, and a uni-traveling carrier photodiode for spectroscopic applications," *J. Lightw. Technol.*, vol. 26, no. 15, pp. 2521–2530, Aug. 2008.

[19] E. Rouvalis, C. C. Renaud, D. G. Moodie, M. J. Robertson, and A. J. Seeds, "Traveling-wave uni-traveling carrier photodiodes for continuous wave THz generation," *Opt. Exp.*, vol. 18, pp. 11105–11110, 2010.

[20] S. Preu, F. H. Renner, S. Malzer, G. H. Döhler, L. J. Wang, M. Hanson, A. C. Gossard, T. L. J. Wilkinson, and E. R. Brown, "Efficient terahertz emission from ballistic transport enhanced n-i-p-n-i-p superlattice photomixers," *Appl. Phys. Lett.*, vol. 90, 2007, Art. ID 212115.

[21] P. Acedo, H. Lamela, S. Garidel, C. Roda, J. P. Vilcot, G. Carpintero, I. H. White, K. A. Williams, M. Thompson, W. Li, M. Pessa, M. Dumitrescu, and S. Hansmann, "Spectral characterisation of monolithic modelocked lasers for mm-wave generation and signal processing," *Electron. Lett.*, vol. 42, pp. 928–929, 2006.

[22] A. R. Criado, P. Acedo, G. Carpintero, C. De Dios, and K. Yvind, "Observation of phase noise reduction in photonically synthesized sub-THz signals using a passively mode-locked laser diode and highly selective optical filtering," *Opt. Exp.*, vol. 20, pp. 1253–1260, 2012.

[23] E. Rouvalis, M. J. Fice, C. C. Renaud, and A. J. Seeds, "Optoelectronic detection of millimetre-wave signals with travelling-wave uni-travelling carrier photodiodes," *Opt. Exp.*, vol. 19, pp. 2079–2084, 2011.

[24] S. Pengbo, N. J. Gomes, P. A. Davies, P. G. Huggard, and B. N. Ellison, "Analysis and demonstration of a fast tunable fiber-ring-based optical frequency comb generator," *J. Lightw. Technol.*, vol. 25, no. 11, pp. 3257–3264, Nov. 2007.

[25] A. R. Johnson, Y. Okawachi, J. S. Levy, J. Cardenas, K. Saha, M. Lipson, and A. L. Gaeta, "Chip-based frequency combs with sub-100 GHz repetition rates," *Opt. Lett.*, vol. 37, pp. 875–877, 2012.

[26] G. Carpintero, M. G. Thompson, R. V. Penty, and I. H. White, "Low noise performance of passively mode-locked 10-GHz quantum-dot laser diode," *IEEE Photon. Technol. Lett.*, vol. 21, pp. 389–391, 2009.

[27] Y. K. Chen, M. C. Wu, T. Tanbun-Ek, R. A. Logan, and M. A. Chin, "Multicolor single-wavelength sources generated by a monolithic colliding pulse mode-locked quantum well laser," *IEEE Photon. Technol. Lett.*, vol. 3, no. 11, pp. 971–973, Nov. 1991.

[28] J. Hasch, E. Topak, R. Schnabel, T. Zwick, R. Weigel, and C. Waldschmidt, "Millimeter-wave technology for automotive radar sensors in the 77 GHz frequency band," *IEEE Trans. Microw. Theory Tech.*, vol. 60, no. 3, pp. 845–860, Mar. 2012.

[29] E. Rouvalis, M. J. Fice, C. C. Renaud, and A. J. Seeds, "Millimeter-wave optoelectronic mixers based on uni-traveling carrier photodiodes," *IEEE Trans. Microw. Theory Tech.*, vol. 60, no. 3, pp. 686–691, Mar. 2012.

[30] T. Yasui, S. Yokoyama, H. Inaba, K. Minoshima, T. Nagatsuma, and T. Araki, "Terahertz frequency metrology based on frequency comb," *IEEE J. Sel. Topics Quantum Electron.*, vol. 17, no. 1, pp. 191–201, Jan.–Feb. 2011.

[31] D. Eliyahu, R. A. Salvatore, and A. Yariv, "Noise characterization of a pulse train generated by actively mode-locked lasers," *J. Opt. Soc. Amer. B, Opt. Phys.*, vol. 13, pp. 1619–1626, July 1996.

[32] D. Eliyahu, R. A. Salvatore, and A. Yariv, "Effect of noise on the power spectrum of passively mode-locked lasers," *J. Opt. Soc. Amer. B, Opt. Phys.*, vol. 14, pp. 167–174, Jan. 1997.

[33] K. Yvind, D. Larsson, L. J. Christiansen, J. Mork, J. M. Hvam, and J. Hanberg, "High-performance 10 GHz all-active monolithic mode-locked semiconductor lasers," *Electron. Lett.*, vol. 40, pp. 735–737, 2004.

A. R. Criado (S'09) received the B.Sc. and M.Sc. degrees in telecommunication engineering and M.Res. degree in advanced electronics systems from Universidad Carlos III de Madrid, Madrid, Spain, in 2009 and 2011, respectively, where he is currently working toward the Ph.D. degree.

He has been involved in research tasks on laser diagnostics for fusion plasmas, specifically electronic density measurement using two color multichannel laser interferometry, and he worked as Collaborator Researcher during 2009 and 2010 with the National Fusion Laboratory, CIEMAT, Spain. His research is in the field of low-noise photonic generation and homodyne/heterodyne detection of mm-waves and sub-THz signals.

C. de Dios received the M.S. degree in applied physics and electronics from the Universidad Complutense of Madrid, Madrid, Spain, and the M.Res. and Ph.D. degrees from the Universidad Carlos III de Madrid, Madrid, Spain, in 2004 and 2010, respectively.

Then, she joined the private sector as a Technical Consultant for Hewlett-Packard. Since 2002, she has been a member of the Optoelectronics and Laser Technology Group at the Universidad Carlos III, Madrid, Spain, where she is currently an Assistant Professor with the Electronics Technology Department. Her research interests are high-speed optical communications, pulsed semiconductor laser sources, nonlinear optical phenomena, and sub-terahertz and millimeter wave photonic signal synthesis and detection.

P. Acedo (M'99) received the B.S. degree in telecommunication engineering from the Universidad Politécnica de Madrid, Madrid, Spain, in 1993, and the Ph.D. degree (with honors) from the Universidad Carlos III de Madrid, Madrid, Spain, in 2000. for his work on heterodyne two color laser interferometry for fusion plasma diagnostics at the Stellarator TJ-II, (Laboratorio Nacional de Fusión, CIEMAT, Madrid) and Tokamak C-Mod (Plasma Science and Fusion Centre, Massachusetts Institute of Technology).

In 2002, he was appointed as an Assistant Professor with the Universidad Carlos III de Madrid, Madrid, Spain, where he has continued with the development of scientific instrumentation systems for fusion plasma diagnostics and biomedical applications. He has been also involved in research on high-speed semiconductor laser devices for microwave and millimeter-wave generation and processing. Currently, his interests in this line are the development of integrated active photonic antennas for mm-wave and THz generation and detection.

G. Carpintero (M'10) received the Ph.D. degree from the Universidad Carlos III de Madrid, Madrid, Spain, in 1999.

Since 2003, he has been an Associate Professor with the Electronic Technology Department, Universidad Carlos III de Madrid, Madrid, Spain. From 2006 to 2009, he was a regular Visiting Scholar with the Engineering Department, University of Cambridge, Cambridge, U.K., where he was involved with quantum-dot mode-locked lasers. He has authored or coauthored a number of papers on semiconductor lasers and microwave photonics. His current research interests include mode-locked lasers, optical frequency synthesis, photonic integrated circuits, and photonic enabled broadband wireless systems.

Dr. Carpintero is member of the Optical Society of America.

K. Yvind received the M.Sc.E. and Ph.D. degrees from the Research Center for Communication, Optics and Materials (COM), Technical University of Denmark, Lyngby, Denmark, in 1999 and 2003.

He is currently an Associate Professor and group leader for Nanophotonic Devices with DTU Fotonik. His working areas cover a broad range of topics from design, cleanroom fabrication, and testing of optical devices in InP, GaAs, and silicon.